Ab initio machine-learning unveils strong anharmonicity in non-Arrhenius self-diffusion of tungsten

Xi Zhang^{1,*}, Sergiy V. Divinski², and Blazej Grabowski¹

¹Institute for Materials Science, University of Stuttgart, D-70569 Stuttgart, Germany

ABSTRACT

We propose an efficient *ab initio* framework to compute the Gibbs energy of the transition state in vacancy-mediated diffusion including the relevant thermal excitations at density-functional-theory level. With the aid of a bespoke machine-learning interatomic potential, the temperature-dependent vacancy formation and migration Gibbs energies of the prototype system body-centered cubic (BCC) tungsten are shown to be strongly affected by anharmonicity. This finding explains the physical origin of the experimentally observed non-Arrhenius behavior of tungsten self-diffusion. A remarkable agreement between the calculated and experimental temperature-dependent self-diffusivity and, in particular, its curvature is revealed. The proposed computational framework is robust and broadly applicable, as evidenced by first tests for a hexagonal close-packed (HCP) multicomponent high-entropy alloy. The successful applications underscore the attainability of an accurate *ab initio* diffusion database.

Introduction

Understanding atomic diffusion is of fundamental importance in developing materials with controlled mechanical and functional properties. For the majority of metals, the temperature dependence of thermally activated, vacancy-mediated diffusion is well assessed from countless studies. The common knowledge expects a linear Arrhenius behavior, especially when phase transformations do not interfere. The logarithm of the diffusion rate, D, scales linearly with the inverse temperature, T^{-1} ,

$$lnD = -(Q/k_{\rm B})T^{-1} + lnD_0,$$
(1)

with the slope, $-Q/k_B$, and the intercept, $\ln D_0$, controlled by the activation energy Q and the prefactor D_0 (k_B : Boltzmann constant). Both Q and D_0 are generally assumed to be *independent* or very weakly dependent on temperature⁶.

The universality of this widespread assumption is, however, limited, especially close to the melting point⁶. Diffusion measurements covering *wide* temperature intervals revealed deviations from linearity^{7–12}. Textbook knowledge explains this "anomaly" of substitutional diffusion with di-vacancies in addition to mono-vacancies^{6, 13, 14}. Various measurements^{15–17} were interpreted as supporting the di-vacancy explanation, which grew into an undisputed paradigm. Nevertheless, some researchers proposed an alternative explanation in terms of temperature-dependent activation energies^{18–22} indicating problems with the mono-/di-vacancy interpretation even in simple metals. Temperature-dependent vacancy formation energies driven by anharmonic vibrations were indeed uncovered by recent *ab initio* simulations^{23, 24}. Temperature-dependent vacancy energies were also found for self-diffusion in Mo²⁵.

These theoretical findings call for a conceptual revision of the long-standing paradigm. However, a paradigm shift requires strong support. Therefore, not only further *ab initio* simulations of defect energetics are required, but in particular methodological advances to enable access to reliable predictions at high temperatures.

While efficient high-accuracy *ab initio* techniques are available for vacancy formation^{23,26}, state-of-the-art *ab initio* approaches approximate migration Gibbs energies by (quasi)harmonic transition state theory (hTST)²⁷, utilizing either the full quasiharmonic free energy²⁸ or a simplified Vineyard formula²⁷ with explicit phonon calculations²⁹. It will be shown below that hTST is unrealistic at elevated temperatures and causes significant errors.

The most accurate approach to exploring the full vibrational space is thermodynamic integration. A crucial requirement for thermodynamic integration is "sufficient" phase stability, i.e., the target phase should be dynamically stable in the temperature

²Institute of Materials Physics, University of Münster, 48149 Münster, Germany

^{*}xi.zhang@imw.uni-stuttgart.de

¹Magnetic^{1,2} or chemical^{3,4} order-disorder transformations might induce characteristic deviations from the Arrhenius-type temperature dependence. Further examples are diffusion non-linearities in β -Ti or Zr near the corresponding $\beta \to \alpha$ transition temperatures⁵.

range of interest. Certain correlated lattice instabilities, e.g., the hcp to dhcp transformation as observed for hcp Ni³⁰, are suppressed by increasing the size of the simulation cell. Other undesirable transformations may be inhibited by restricting the cell to smaller sizes³¹. For an intrinsically localized instability as experienced by a diffusing atom at the energetic saddle point such measures will not be effective. Although finite-temperature path-based approaches such as the finite temperature string method³² and the mean-force based integration^{33,34} have been developed to include the full vibrational contribution to the activation free energy, their practical application in an ab initio framework is not feasible.

Here, we propose an efficient and accurate ab initio method that overcomes the dynamical instability problem of the transition state. We show that with the introduced stabilization scheme—implemented in a machine-learning-assisted thermodynamicintegration + direct-upsampling framework—the full temperature dependence of vacancy migration Gibbs energies can be efficiently calculated, including all relevant thermal excitations with density-functional-theory (DFT) accuracy. Together with the vacancy formation Gibbs energies, likewise computable with the direct upsampling technique, accurate ab initio self-diffusivities become available, even for high melting systems.

Results and discussion

Transition state thermodynamic integration

Figure 1 provides the general workflow of the introduced transition state thermodynamic integration (TSTI) approach. The key parts are highlighted by the gray-blue boxes. At the core lies the actual TSTI calculation from a stabilized dynamical matrix to a highly optimized machine-learning potential, specifically a moment tensor potential (MTP)³⁵. The TSTI calculation is followed by direct upsampling to achieve DFT accuracy.

The MTP is trained on a large DFT dataset (2591 structures) including bulk, vacancy, and transition-state configurations sampled from high-temperature MD. The root-mean-square error (RMSE) is only 1.9 meV/atom in energies and 0.15 eV/Å in forces, respectively. Consequently, the MD energies (2591 energies in total) and forces (nearly one million forces in total) predicted by the MTP show a strong correlation with the DFT data, cf. Figure 2. The good performance of the MTP ensures an accurate description of the vibrational phase space for the considered bulk, vacancy, and transition-state configurations and boosts up the direct upsampling convergence. More details about the MTP are given in the Supplementary Material.

The anharmonic free energy is expressed as

$$F^{\rm ah} = \Delta F_{\rm MTP}^{\rm qh \to full} + \Delta F_{\rm DFT}^{\rm up},\tag{2}$$

where the first term $\Delta F_{MTP}^{qh o full}$ is obtained from the TSTI calculation to the MTP and the second term ΔF_{DFT}^{up} from free energy perturbation theory, i.e., the direct upsampling, to DFT. Specifically,

$$\Delta F_{\text{MTP}}^{\text{qh}\to\text{full}} = \int_{0}^{1} d\lambda \, \langle E_{\text{s}}^{\text{full}}(\{\mathbf{R}_{I}\}) - E^{\text{qh}}(\{\mathbf{R}_{I}\}; \underline{\underline{\mathcal{D}}_{\text{s}}}) \rangle_{\lambda} \tag{3}$$

represents a thermodynamic integration along the coupling parameter $\lambda \in [0,1]$, with the thermodynamic average $\langle ... \rangle_{\lambda}$ of the difference between the quasiharmonic energy $E_s^{\rm qh}$ and the *stabilized* full vibrational MTP energy $E_s^{\rm full}$ (discussed below) computed for different configurations of the atomic coordinates $\{\mathbf{R}_I\}$. For each fixed value of λ , the atomic movement in the MD simulation is driven by forces derived from a linear combination of quasiharmonic and MTP forces.

A key ingredient to the here proposed approach is the *stabilized* dynamical matrix \mathcal{D}_s computed from the original, unstable

$$\underline{\underline{\mathcal{D}}}_{s} = \underbrace{\underline{\underline{\mathbf{w}}} \cdot \underline{\underline{\mathbf{w}}}^{2} \cdot \underline{\underline{\mathbf{w}}}^{-1}}_{3N-1 \text{ stable modes}} + \underbrace{\underline{\underline{\mathbf{w}}} \cdot \underline{\underline{\mathbf{w}}}_{s}^{2} \cdot \underline{\underline{\mathbf{w}}}^{-1}}_{1 \text{ stabilized mode}}, \tag{4}$$

where
$$\underline{\underline{\boldsymbol{\omega}^2}} = \operatorname{diag}(\boldsymbol{\omega}_1^2, ..., \boldsymbol{\omega}_{3N-1}^2, 0),$$
 (5)

$$\underline{\omega_{s}^{2}} = \operatorname{diag}(0, ..., 0, \alpha | \omega_{\text{imag}}^{2} |) \tag{6}$$

represent two $3N \times 3N$ diagonal matrices, which store the 3N-1 stable phonon frequencies ω_i and the single *stabilized* phonon frequency, respectively. The stabilization is achieved by taking the absolute value of the reaction coordinate frequency $\omega_{\rm imag}^2$ times a tunable parameter α . Further in Eq. (4), w is the eigenvector matrix of the original, unstable dynamical matrix.

The second crucial ingredient to our scheme is the stabilization of the MTP forces during the thermodynamic integration. This is achieved by replacing the forces along the unstable mode with the *stabilized* harmonic forces given by $\underline{\mathcal{D}}_s$. Specifically, for a given λ , the interatomic forces are obtained as

$$\mathcal{F}_{\lambda} = (1 - \lambda)\mathcal{F}_{s}^{qh} + \lambda\mathcal{F}_{s}^{MTP}, \tag{7}$$

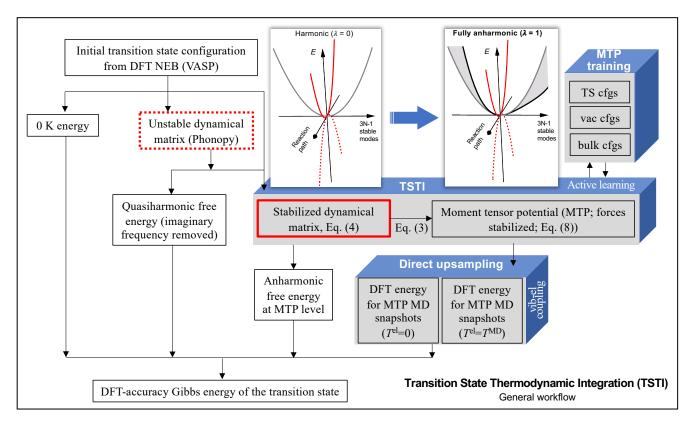


Figure 1. TSTI Workflow. Schematic illustration of the proposed transition state thermodynamic integration (TSTI) approach (NEB = nudged elastic band; TS = transition state; cfgs = configurations (sampled from MD); T^{el} = electronic temperature).

with the forces \mathcal{F}_s^{qh} corresponding to $\underline{\mathcal{D}}_s$ and with the *stabilized* MTP forces \mathcal{F}_s^{MTP} computed by

$$\mathcal{F}_{s}^{MTP} = \mathcal{F}^{MTP}(\{\mathbf{R}_{I}\}) + [\mathcal{F}_{s}^{qh}(\{\mathbf{R}_{I}^{sp} + \mathbf{u}_{I}'\}) - \mathcal{F}^{MTP}(\{\mathbf{R}_{I}^{sp} + \mathbf{u}_{I}'\})], \tag{8}$$

where $\mathcal{F}^{\mathrm{MTP}}$ are the original unstabilized forces and

$$\mathbf{u}_{I}' = (\mathbf{u}_{I} \cdot \hat{\mathbf{w}}_{imag}) \cdot \hat{\mathbf{w}}_{imag}, \quad \mathbf{u}_{I} = \mathbf{R}_{I} - \mathbf{R}_{I}^{sp}, \tag{9}$$

with the saddle-point positions $\{\mathbf{R}_I^{\mathrm{sp}}\}$ and the normalized eigenvector $\hat{\mathbf{w}}_{\mathrm{imag}}$ of the unstable phonon mode. Consistently, the corresponding MTP potential energy entering Eq. (3) is computed as

$$E_{s}^{\text{full}}(\{\mathbf{R}_{I}\}) = E^{\text{full}}(\{\mathbf{R}_{I}\}) + [E^{\text{qh}}(\{\mathbf{R}_{I}^{\text{sp}} + \mathbf{u}_{I}'\}; \underline{\mathcal{D}}_{s}) - E^{\text{full}}(\{\mathbf{R}_{I}^{\text{sp}} + \mathbf{u}_{I}'\})], \tag{10}$$

where E^{full} is the original unstabilized MTP potential energy.

The TSTI workflow relies upon and significantly advances the established computational framework for high-accuracy *ab initio* Gibbs energies for equilibrium states [36]. In particular, as highlighted by the two schematic plots in Figure 1, the unstable mode (red dotted line), which drives the saddle-point configuration to the equilibrium, does not contribute to the vibrational free energy of the transition state. This mode can be modified to a stable mode without altering the free energy. Specifically, at $any \lambda$, the instability is replaced by the stable energy profile corresponding to $\alpha |\omega_{\text{imag}}^2|$ (red solid line). Since the stabilized energy profile along the thermodynamic-integration path remains unchanged, there is no explicit contribution of the reaction coordinate to the free energy difference in Eq. (2). (This is consistent with hTST in sampling the (3N-1) stable modes, albeit in the harmonic regime.) The stabilization in TSTI is of crucial importance to restrict the vibrations to the vicinity of the saddle point, such as to enable the sampling of the anharmonicity (gray shaded area) from all other, 3N-1 stable modes (gray or black curves).

With TSTI, the anharmonicity of the transition state is captured at the accuracy level of the MTP. Upsampling based on molecular-dynamics snapshots with the full free-energy formula for $\Delta F_{\rm DFT}^{\rm up}$ ensures DFT accuracy. Electronic excitations and their coupling to atomic vibrations are computed in a second upsampling step utilizing finite temperature DFT^{36,37}. Thus, the full set of free energy contributions can be computed for the transition state at the level of DFT accuracy.

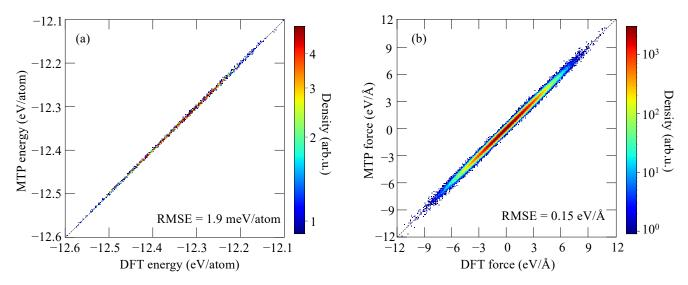


Figure 2. Accuracy of the moment tensor potential (MTP). Correlation plots of the energies (a) and forces (b) of the MTP vs. DFT and the corresponding root-mean-square errors (RMSEs).

Temperature-dependent Gibbs energies of vacancy formation and migration

We use TSTI to calculate the Gibbs energy of vacancy migration $G_{\rm mig}(T)$ for BCC W. The reference transition-state configuration, $\{{\bf R}_I^{\rm sp}\}$, is obtained from the climbing-image nudged elastic band³⁸ method performed at zero Kelvin. At high temperatures, even close to the melting point, the MD migration trajectories suggest that, for symmetrical crystalline structures like BCC, the migration pathway remains the same (see Figure S6 in the Supplementary Material and the related discussion). For complex molecular systems³⁹, migration pathways may be modified at high temperatures due to fewer symmetry restrictions, which would require a special analysis that is out of the scope of the present paper. We use the "standard" scheme of thermodynamic-integration + direct-upsampling^{36,40} to calculate the Gibbs energy of vacancy formation $G_{\rm form}(T)$. The self-diffusion coefficient reads

$$D(T) = a_0^2(T) f_{\text{bcc}} \frac{k_{\text{B}} T}{h} \exp\left(-\frac{G_{\text{form}}(T) + G_{\text{mig}}(T)}{k_{\text{B}} T}\right),\tag{11}$$

where h is the Planck constant. The lattice constant at zero pressure $a_0(T)$ is obtained from the relative thermal expansion (DFT molecular dynamics) reported in Ref. [41] and rescaled with the lattice constant at 0 K, 3.1723 Å, calculated here (see Supplementary Material for more details). The correlation factor for vacancy diffusion on the BCC lattice, f_{bcc} , takes the value of 0.7272^{42} . For the DFT calculations, we employ the projector augmented wave (PAW) method⁴³ within the generalized gradient approximation (GGA) in the Perdew-Burke-Ernzerhof (PBE) parametrization⁴⁴ as implemented in VASP^{45,46}. Further details are given in the Supplementary Material.

Figure 3 presents the temperature-dependent Gibbs energies of vacancy formation and migration for BCC W. The red circles and lines correspond to the final Gibbs energies with all thermal contributions included. For both $G_{\text{form}}(T)$ and $G_{\text{mig}}(T)$, a strong and clearly *non-linear* temperature dependence is observed, particularly in the temperature range where diffusion is measured ($T > 0.46 T^{\text{melt}}$, gray shaded area). The computed high-temperature data are well reproduced by a quadratic fit (red solid lines), as observed before for formation Gibbs energies²³. The energy reduction with temperature is particularly strong for vacancy formation and reaches -1.21 eV (-36%) at 3400 K as compared to the 0 K value.

The experimental data (black symbols) reflect extrapolations of high-temperature measurements utilizing the *linear* Arrhenius ansatz, i.e., $G_{\text{form/mig}} = H_{\text{form/mig}} - TS_{\text{form/mig}}$, with temperature-independent enthalpies ($H_{\text{form/mig}}$) and entropies ($S_{\text{form/mig}}$) of formation/migration. Although such a linear fitting ansatz is clearly inappropriate based on the present and previous results^{23, 24}, we utilize it nevertheless to fit our exact data for the purpose of an unbiased comparison between theory and experiment. For both formation and migration, a linear Arrhenius fit of the full Gibbs energies between 2400 K and 2800 K shows good agreement with experiment, considering the significant scatter and uncertainty in the high-temperature

A comparison between the generally applied quasiharmonic approximation (gray diamonds) and the Gibbs energies featuring full vibrations (blue squares) unveils strong anharmonicity in the formation and migration of a vacancy. The Gibbs energies decrease significantly due to explicit anharmonicity as highlighted by the arrows labeled "ah"; max. -20% for the

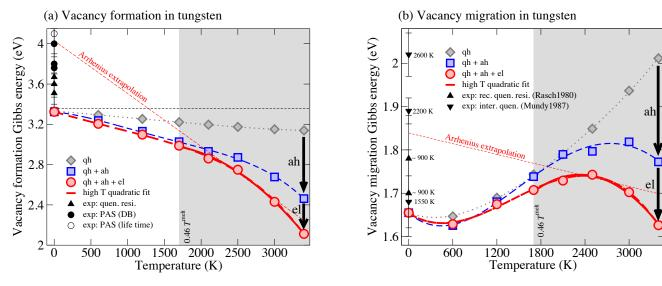


Figure 3. Impact of anharmonicity and electrons on vacancy formation and migration in tungsten. (a) Formation and (b) migration Gibbs energies from the proposed TSTI approach in comparison with experiments. Experimental techniques: (a): quenched-in resistivity^{47–49}, positron annihilation spectroscopy (PAS) Doppler broadening (DB)^{50–52} and life time⁵¹; (b): recovery of quenched-in resistivity⁴⁸ and interrupted quenching²⁰. The dotted/dashed lines connecting the computed data points (filled symbols) are fourth-order polynomial fits. The dashed red lines show the linear Arrhenius extrapolation of the Gibbs energies from the temperature range of 2400 K to 2800 K.

vacancy formation and -15% for the migration. The strong non-linear temperature dependence observed for the full vibrational Gibbs energies is absent for the quasiharmonic approximation. This highlights that the so far well-established and generally applied quasiharmonic approximation is not adequate to describe the vibrational contribution in vacancy-mediated diffusion.

Strong impact of electronic excitations

Electronic excitations have traditionally been considered less influential in state-of-the-art diffusion studies²⁹. Thus in practice, explicit calculations of electronic free energy have often been omitted^{29,53,54} or, when considered, relied on the ideal static lattice approximation⁵⁵.

The present computational framework enables us to explicitly account for electronic excitations and the coupling effect with thermal vibrations. As revealed in Figure 3, electronic excitations including the coupling to vibrations provide a sizable contribution to the Gibbs energies (black arrows labeled with "el"). The corresponding decrease is -0.35 eV for the vacancy formation and -0.15 eV for the migration Gibbs energy.

The electronic impact can be understood from an analysis of the electronic density of states. Figure 4 shows the electronic density of states (eDOS) at 3000 K extracted from molecular dynamics snapshots. The smoothening effect due to thermal vibrations (i.e., decrease of peaks and increase of valleys as the one close to the Fermi level) becomes stronger with the sequence of bulk to vacancy to transition state, as is observed from the mean eDOS's (solid lines in blue, red, black, respectively) each averaged over 120 MD snapshots (the lighter background with similar color tone). Despite the considerable variance in the eDOS's of the single snapshots, the standard errors of the mean values are about one order of magnitude smaller than the differences between the different types of structures (bulk, vacancy, and transition state) in particular at the valleys and peaks (see Figure S4 in Supplementary Material), suggesting that the eDOS's are well converged. At high (electronic) temperatures, the Fermi function (dash-dotted curve shown in the right panel) re-populates the electrons from below the Fermi level to higher energy states above the Fermi level. The resulting holes and excited electrons are the origin of the electronic entropy contribution to the free energy. A *large* eDOS at the Fermi level facilitates many such excitations and thus implies a *largely negative* electronic free energy, as detailed in Ref. [56]. As observed around the valley region enlarged in the right panel of Figure 4, the eDOS's close to the Fermi level increase with the sequence of bulk to vacancy to transition state. As a consequence, a more negative free energy contribution can be expected for both vacancy formation and migration Gibbs energies as indeed seen in Figure 3.

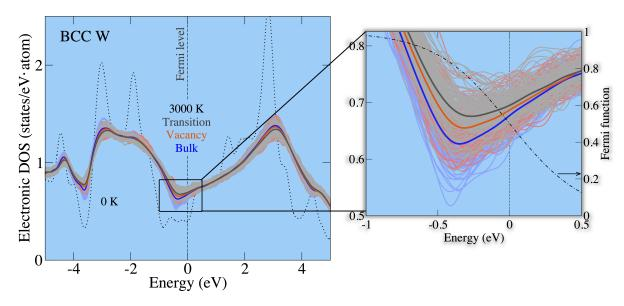


Figure 4. Origin of the strong impact of electronic excitations. The mean electronic densities of states of the bulk structure (blue), the vacancy structure (red), and the transition state structure (black) at 3000 K are shown. The corresponding DOS's of 120 MD snapshots from which the mean DOS is obtained are plotted in the background in a lighter version of the respective color. The right panel shows the enlarged view of the valley close to the Fermi level. The dash-dotted curve indicates the Fermi function at 3000 K.

Collective motion of the migrating atom and its neighborhood

For the vacancy formation process, the physical origin of anharmonicity is well understood within the local Grüneisen theory 23 . The here developed TSTI approach allows us to also access the full vibrational space of the transition state of vacancy migration. To understand the underlying physics of the strong anharmonicity, we collect long-time molecular-dynamics trajectories for 3×10^5 steps (1.5 nanoseconds) and examine the relative motion of the migrating atom with respect to its first and second neighbors. The geometrical relations are shown in Figure 5(a). In Figure 5(c)–(f), we plot the projection of the displacements of the 1^{st} (2^{nd}) neighbor atom onto $\mathbf{v_1}$ ($\mathbf{v_2}$) versus the projection of the migrating atom onto $-\mathbf{v_1}$ ($\mathbf{v_3}$). The vectors $\mathbf{v_1}$ and $-\mathbf{v_1}$ lie opposite to each other along the line connecting the migrating atom and the 1^{st} neighbor atom. The vectors $\mathbf{v_2}$ and $\mathbf{v_3}$ are directed towards the vacancy center ($\langle 111 \rangle$ direction).

As seen from Figure 5, the full vibrations ((c) and (d)) and the harmonic approximation ((e) and (f)) describe different scenarios in terms of the distribution of the relative motion. For the interaction with the first neighbor, we observe the breakdown of harmonic symmetry due to Pauli repulsion as found previously for bulk anharmonicity⁵⁷. The motion of the two atoms towards each other is energetically disfavored (suppressed distribution in quadrant I in (c)), whereas the motion away from each other is favored (increased distribution in quadrant III). This distinctive feature of the fully anharmonic potential cannot be described by any harmonic potential since the latter will always enforce the same energy profile whether two atoms move to or away from each other.

For the interaction of the second neighbor with the migrating atom (Figure 5(d)), we observe likewise strong anharmonicity. The distribution function is very skewed along the positive v_3 vector. This means that the motion of the second neighbor toward the vacancy is energetically preferred. Effectively, the second neighbor is drawn into the vacant site. Such preferential inward vibrations of atoms next to a vacancy were reported for vacancy *formation*²³. With the presence of the migrating atom at the saddle point, most interestingly and not reported so far, such an anharmonic inward motion of the 2^{nd} neighbor atom is significantly correlated with the motion of the migrating atom: it is particularly favored when the migrating atom moves away from the vacancy (toward the other vacant site), as is shown by the non-symmetric distributions in quadrant I and II of Figure 5(d) and highlighted by the yellow arrows in the real-time MD trajectory depicted in Figure 5(b). These anharmonic characteristics are completely absent in the harmonic distributions. Note that such a concerted motion of a group of atoms might be favored for shallow potential landscapes, as it is anticipated for diffusion in melts⁵⁸, amorphous materials⁵⁹, or even for grain boundary diffusion⁶⁰.

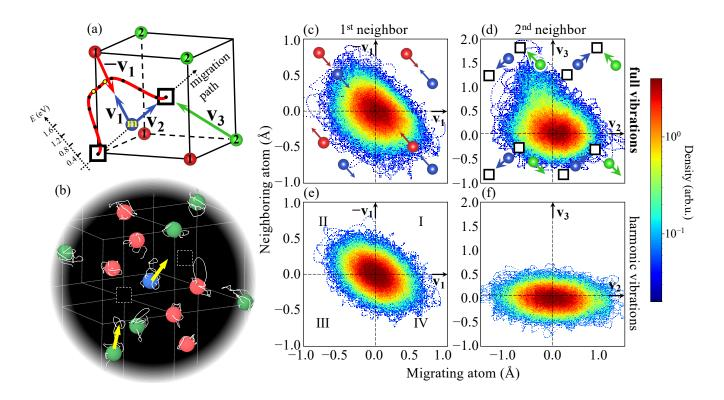


Figure 5. Collective motion of migration atom and its neighborhood. (a) Migrating atom (blue atom labeled with "m") and its local environment (red atoms: 1st neighbors; green atoms: 2nd neighbors) in the transition state. The red energy profile shows the calculated NEB minimum energy path marked with the intermediate images (black dots) and the saddle points (yellow dots). (b) Real-time MD trajectory (the white line associated with each atom) of a short time frame of 300 MD steps (yellow arrows highlight the directions of the collective motion). (c–f) Distribution of the correlated vibrations of the migrating atom with its first (1st column) and second (2nd column) neighbor accounting for the full anharmonic interactions (1st row) and quasiharmonic interactions only (2nd row). The trajectory in (b) and the distribution functions in (c–f) correspond to MTP molecular dynamics at 3400 K and at the corresponding lattice constant of 3.24 Å.

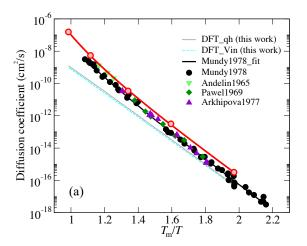
Non-Arrhenius self-diffusion of tungsten

The Arrhenius plot of the calculated self-diffusion is shown in Figure 6 (a) as a function of the inverse homologous temperature², and compared with the most reliable experiments^{12,64–66}. The strong non-linear temperature dependence of the diffusion coefficient is revealed in Figure 6(b). The full DFT results agree very well with experiment. In contrast, the diffusivity derived from the (quasi)harmonic approximation (hTST; including the simplified Vineyard formula) yields an incorrect linear behavior. As the present DFT quasiharmonic results take the thermal expansion effect fully into account, the lattice expansion, previously proposed to explain the non-Arrhenius behavior⁶⁷, plays a negligible role in the high-temperature non-Arrhenius diffusion of W. We conclude instead that the non-Arrhenius self-diffusion of tungsten originates from strong anharmonicity in both the formation and migration of mono-vacancies. Since the calculations are based on the single mono-vacancy mechanism, the consistent curvature of the full DFT results with experiment indicates that the alternative di-vacancy mechanism plays a minor role in the non-Arrhenius diffusion of tungsten. A detailed analysis of the di-vacancy hypothesis, likewise leading to the exclusion of this mechanism, is provided in the Supplementary Material. We attribute the remaining discrepancy of the computed diffusion coefficient with experiment (Figure 6(a) and Figure S4) to the employed exchange-correlation functional and experimental uncertainties.

General applicability of TSTI

As the key ingredients of TSTI, i.e., the stabilization of the dynamical matrix and the MTP forces, are *system-independent* in their construction, the TSTI approach can be applied to diffusion in metals and alloys of any crystalline structure. Although we

 $^{^2}$ We use the DFT-PBE predicted melting point of 3349 K 61 for the present DFT results and the experimental melting point of 3687 K from the CRC Handbook 62 for the experimental data. The Arrhenius plot on the inverse homologous temperature scale compensates for the significant discrepancy (more than 300 K) between the DFT (GGA-PBE) predicted melting point and the experimental melting point for BCC W, as discussed in Ref. [63]. A corresponding plot on the absolute temperature scale is provided in the Supplementary Material.



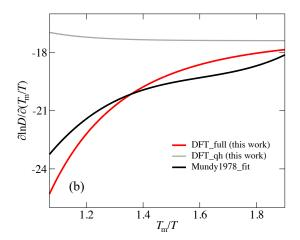


Figure 6. Non-Arrenius self-diffusion of tungsten. (a) Arrhenius plots of self-diffusivity in BCC tungsten calculated with the proposed *ab initio* machine-learning TSTI approach with all finite-temperature excitations taken into account (red circles and lines) on the homologous temperature scale in comparison to experimental data from Mundy et al. ¹², Andelin et al. ⁶⁴, Pawel et al. ⁶⁵, and Arkhipova et al. ⁶⁶. (b) A comparison of the temperature-dependent slopes of the Arrhenius plots in (a).

have focused in this work primarily on the self-diffusion of tungsten, applications of TSTI to more complex systems such as five-component high-entropy alloys (HEAs) are on their way. Previous studies^{68,69} have demonstrated that MTPs are efficient and accurate in describing the vibrational phase space, even for such complex multicomponent systems. The achievable root-mean-square errors of only 2–3 meV/atom are the foundational premise for the success of direct upsampling.

To prove the general applicability of TSTI for complex HEAs with different crystalline structures other than BCC W, we show preliminary results in the Supplementary Material for a new category of hexagonal close-packed (HCP) HEAs, $Al_{15}Hf_{25}Sc_{10}Ti_{25}Zr_{25}$, which exhibit promising mechanical properties⁷⁰ and intriguing defect and diffusion properties in experiment and theory^{71–74}. An accurate MTP with an RMSE of 2.5 meV/atom has been developed. The resulting well-behaved $\langle E^{\text{full}} - E^{\text{qh}} \rangle_{\lambda}$ curve (Figure S7(a)) and the stable MD trajectory of the migrating atom (Zr) at the transition state (Figure S7(b)) substantiate the broad applicability and the robust performance of the TSTI approach. A complete simulation study of the diffusion in HEAs with DFT accuracy requires an increased computational effort due to the additional chemical complexity. Statistical sampling in both configurational and vibrational degrees of freedom must be performed and converged to obtain reasonable diffusivities. Such an investigation goes beyond the scope of the present study and is the focus of a separate project.

Concluding remarks and outlook

Utilizing a bespoke machine-learning potential, we have developed an efficient *ab initio* framework, the *transition state thermodynamic integration* (TSTI) approach, to accurately compute the Gibbs energy of the transition state. The inherent dynamical instability—so far limiting the use of thermodynamic integration—has been successfully overcome.

We have applied the proposed framework to predict the temperature-dependent vacancy migration and formation Gibbs energies of BCC W, revealing strong anharmonic atomic vibrations. The resulting migration and formation Gibbs energies exhibit a significant non-linear temperature dependence. Through the analysis of long-time molecular-dynamics trajectories, we have found that the strong anharmonicity originates from a non-symmetric relative motion of the first and the second neighbor atoms with respect to the migrating atom at the transition state. The predicted temperature-dependent self-diffusion coefficient shows clearly a non-Arrhenius curvature and agrees remarkably well with experimental data on the inverse homologous temperature scale. In contrast, the generally applied quasiharmonic approximation cannot explain the observed non-Arrhenius behavior.

The developed framework opens new avenues in probing the diffusion behavior with *ab initio* accuracy, including transition states in the whole temperature range. It allows us to understand observed diffusion anomalies and resolve long-standing and highly debated problems. Diffusion properties of metastable and unstable phases become computable with density-functional-theory accuracy, which is of paramount importance for consistent and reliable development of (CALPHAD-type) mobility databases with end-members for which no experimental data exist (like BCC Al or Ni for the assessment of mobilities in the B2 NiAl phase relevant to Ni-based superalloys). In particular, for dynamically unstable phases where the relaxation of vacancy-containing structures and also the nudged-elastic-band method become infeasible due to the instability, the present computational framework, which combines TSTI with direct upsampling, provides a unique advantage to treat such phases if

they can be dynamically stabilized in molecular dynamics at elevated temperatures. Once a proper reference potential with known free energy is available, TSTI from the reference potential to the full vibrational potential (moment tensor potential (MTP) in this work) can be applied to obtain the anharmonic free energy contribution, followed by direct upsampling to achieve the full density-functional-theory accuracy. Possible references are, for example, the effective harmonic potential or the Einstein solid for the stable end-points of diffusion⁷⁵ and a migration path interpolated from stable reference elements for the transition state⁶⁷.

With the increasing importance of diffusion data in developing advanced materials, accurate theoretical prediction of diffusivities is highly desirable. As the introduced methodology is general, it can be extended beyond vacancy-mediated diffusion to transition-state Gibbs energies of other diffusion mechanisms. We have shown that it can be applied to complex alloy systems such as high-entropy alloys where the Gibbs energy contribution to diffusion from the configurational degree of freedom also shows a non-Arrhenius behavior⁷⁴. Stabilized molecular-dynamics trajectories for the migrating atom at the transition state in a five-component HCP high-entropy-alloy system support the applicability of TSTI. The introduced and verified TSTI approach is straightforward to implement in a standard thermodynamic-integration code, and it can be thus suggested for community usage and versatile testing in other applications, particularly in studies of diffusion-controlled processes. As an ultimate goal, a comprehensive physics-informed accurate *ab initio* diffusion database can be expected.

Methods

General ab initio free energy approach for defects

The temperature-dependent Gibbs energies of vacancy formation and migration for pure metals are expressed as

$$G_{\text{form}}(T) = G_{\text{vac}}(T) - \frac{N-1}{N}G_{\text{bulk}}(T)$$
(12)

and

$$G_{\text{mig}}(T) = G_{\text{TS}}(T) - G_{\text{vac}}(T), \tag{13}$$

where G_{bulk} , G_{vac} , and G_{TS} are the Gibbs energies of the perfect bulk, vacancy and transition-state supercell, and N is the number of atoms in the perfect bulk supercell. At the equilibrium volume of a given temperature (zero pressure), the Gibbs energy and the Helmholtz energy coincide. To account for the various relevant temperature-dependent thermal excitations, the Helmholtz energy is adiabatically decomposed as 26

$$F(V_{eq}(T),T) = E_{0K}(V_{eq}(T=0K)) + F^{qh}(V_{eq}(T),T) + F^{ah}(V_{eq}(T),T) + F^{el}(V_{eq}(T),T),$$
(14)

where E_{0K} denotes the 0 K total energy, F^{qh} and F^{ah} the contribution from non-interacting phonons (quasiharmonicity) and from *explicit* phonon-phonon interactions (anharmonicity), respectively. Further, F^{el} refers to the electronic free energy with the impact of thermal vibrations taken into account. All free energy contributions correspond to the equilibrium volume $V_{eq}(T)$ at temperature T according to the thermal expansion.

Quasiharmonic free energy F^{qh}

The quasiharmonic free energy is calculated by applying the Bose-Einstein statistics to populate the phonon energy levels, i.e.,

$$F^{\rm qh} = \sum_{i}^{3N} \left\{ \frac{\hbar \omega_i}{2} + k_{\rm B} T \ln \left[1 - \exp\left(-\frac{\hbar \omega_i}{k_{\rm B} T}\right) \right] \right\},\tag{15}$$

with the reduced Planck constant \hbar and phonon frequencies ω_i . The finite-displacement supercell approach⁷⁶ is used to extract phonon frequencies, as implemented in phonopy⁷⁷.

For the transition state, the integration of phonon modes in Eq. (15) excludes the single imaginary mode along the reaction path, as described in the conventional harmonic transition state theory (hTST)²⁷.

Explicitly anharmonic free energy F^{ah}

• Thermodynamic integration The explicitly anharmonic free energy F^{ah} , i.e., the difference between the full vibrational free energy and the quasiharmonic free energy, can be extracted by applying a thermodynamic integration (for bulk and vacancy configuration) or the proposed *transition state thermodynamic integration* (TSTI; for the transition state) along a predefined thermodynamic pathway between the quasiharmonic potential, E^{qh} , and the full vibrational

potential, e.g, the moment tensor potential (MTP) E^{MTP} in this work. In practice, the thermodynamic path is usually established by a linear interpolation, i.e.,

$$E_{\lambda} = (1 - \lambda)E^{\text{qh}} + \lambda E^{\text{MTP}},\tag{16}$$

where λ is a coupling parameter with a value between 0 and 1. For different λ , the atomic movement in the MD simulations is driven by forces described by either $E^{\rm qh}(\lambda=0)$ or $E^{\rm MTP}(\lambda=1)$ or a linear mixing of both $E_{\lambda}(0<\lambda<1)$. The anharmonic free energy then reads

$$F^{ah} = \int_0^1 d\lambda \left\langle \frac{\partial E_\lambda}{\partial \lambda} \right\rangle_{\lambda} = \int_0^1 d\lambda \left\langle E^{MTP} - E^{qh} \right\rangle_{\lambda} + \Delta F^{up}, \tag{17}$$

where $\langle ... \rangle$ refers to the thermal average and the remaining minor free energy adjustment ΔF^{up} required for full DFT accuracy can be obtained from direct upsampling⁶⁹.

• **Direct upsampling** The free energy difference between MTP and DFT can be calculated in a perturbative manner using the free-energy perturbation expression, as given by,

$$\Delta F^{\rm up} = -k_{\rm B}T \ln \left\langle \exp\left(-\frac{E^{\rm DFT} - E^{\rm MTP}}{k_{\rm B}T}\right) \right\rangle_{\rm MTP},\tag{18}$$

where $k_{\rm B}$ is the Boltzmann constant and $E^{\rm DFT}$ and $E^{\rm MTP}$ are DFT and MTP energies of molecular dynamics snapshots obtained from MTP trajectories.

Electronic free energy including thermal vibration coupling effects

Due to the accurate MTP forces as compared to DFT (Figure 2(b)), the free energy perturbation theory can also be applied to capture the free energy difference between DFT with and without electronic excitations utilizing the MD snapshots generated by the MTP. The electronic free energy, including the coupling effects, can be taken into account by setting the electronic temperature in the DFT calculations to the respective molecular dynamics temperature³⁶, i.e.,

$$F^{\text{el}} = -k_{\text{B}}T\ln\left\langle \exp\left(-\frac{E_{\text{el}}^{\text{DFT}} - E^{\text{DFT}}}{k_{\text{B}}T}\right)\right\rangle_{\text{MTP}}.$$
(19)

Moment tensor potentials

To boost up the TSTI calculations, we employ the moment tensor potential (MTP)³⁵. MTP utilizes moment tensor descriptors to characterize the local atomic environment n_i :

$$M_{\mu,\nu}(n_i) = \sum_{j} f_{\mu}(|r_{ij}|, z_i, z_j) \underbrace{\mathbf{r}_{ij} \otimes \dots \otimes \mathbf{r}_{ij}}_{\nu \text{ times}}, \tag{20}$$

where the radial function f_{μ} encapsulates information about relative atomic distances ($|r_{ij}|$) and chemical types (z_i, z_j), while the angular part $r_{ij} \otimes ... \otimes r_{ij}$ represents the moments of inertia. The potential energy is expressed as the sum of contributions from all local environments, i.e., $E^{\text{MTP}} = \sum_i V(n_i) = \sum_i \sum_{\alpha} \xi_{\alpha} B_{\alpha}(n_i)$, where B_{α} denotes basis functions derived from contractions of the moment tensors, and ξ_{α} represents linear fitting parameters.

Data availability

The authors declare that all data supporting the findings are available from the corresponding author upon reasonable request.

Code availability

The authors declare that the custom codes/software for the transition state thermodynamic integration are available from the corresponding author upon reasonable request.

References

- **1.** Iijima, Y. Diffusion in high-purity iron: Influence of magnetic transformation on diffusion. *J. Phase Equilibria Diffusion* **26**, 466–471, DOI: 10.1016/S1359-6454(96)00196-6 (2005).
- **2.** Hegde, O. *et al.* Impact of magnetic transition on Mn diffusion in α-iron: Correlative state-of-the-art theoretical and experimental study. *Phys. Rev. B* **104**, 184107, DOI: 10.1103/PhysRevB.104.184107 (2021).
- **3.** Iijima, Y. & Lee, C.-G. Self-diffusion in b.c.c. and ordered phases of an equiatomic iron-cobalt alloy. *Acta Metall. et Materialia* **43**, 1183–1188, DOI: 10.1016/0956-7151(94)00331-B (1995).
- **4.** Tokei, Z., Bernardini, J., Gas, P. & Beke, D. Volume diffusion of iron in Fe₃Al: Influence of ordering. *Acta Materialia* **45**, 541–546, DOI: 10.1016/S1359-6454(96)00196-6 (1997).
- 5. Heiming, A. *et al.* Phonons and martensitic phase transitions in pure bcc Ti and bcc Zr. *Phys. Rev. B* 40, 11425–11428, DOI: 10.1103/PhysRevB.40.11425 (1989).
- **6.** Mehrer, H. *Diffusion in Solids: Fundamentals, Methods, Materials, Diffusion-Controlled Processes.* Springer series in solid-state sciences (Springer, Berlin, Heidelberg, 2007).
- 7. Murdock, J., Lundy, T. & Stansbury, E. Diffusion of Ti44 and V48 in titanium. *Acta Metall.* **12**, 1033–1039, DOI: https://doi.org/10.1016/0001-6160(64)90075-6 (1964).
- **8.** Bakker, H. A Curvature in the In D versus 1/T Plot for Self-Diffusion in Nickel at Temperatures from 980 to 1400°C. *Phys. Status Solidi* (*b*) **28**, 569–576, DOI: https://doi.org/10.1002/pssb.19680280214 (1968).
- 9. Seeger, A. & Schumacher, D. On the analysis of nonlinear Arrhenius plots of self-diffusion coefficients for f.c.c. metals. *Mater. Sci. Eng.* 2, 31–36, DOI: https://doi.org/10.1016/0025-5416(67)90041-9 (1967).
- **10.** Backus, J. G. E. M., Bakker, H. & Mehrer, H. Self-diffusion measurements in silver at low temperatures using single crystals and slightly deformed crystals. *Phys. Status Solidi* (b) **64**, 151–162, DOI: https://doi.org/10.1002/pssb.2220640119 (1974).
- **11.** Maier, K. Self-diffusion in copper at "low" temperatures. *Phys. Status Solidi* (*a*) **44**, 567–576, DOI: https://doi.org/10. 1002/pssa.2210440220 (1977).
- **12.** Mundy, J. N., Rothman, S. J., Lam, N. Q., Hoff, H. A. & Nowicki, L. J. Self-diffusion in tungsten. *Phys. Rev. B* **18**, 6566–6575, DOI: 10.1103/PhysRevB.18.6566 (1978).
- 13. Adda, A. & Philibert, J. La diffusion dans les solides (Presses Universitaires de France, Saclay, 1966).
- **14.** Seeger, A. & Mehrer, H. Diffusion in solids. In Seeger, A., Schumacher, D., Diehl, J. & Schilling, W. (eds.) *Vacancies and Interstitials in Metals* (North-Holland, Amsterdam, 1970).
- **15.** Beyeler, M. & Adda, Y. Détermination des volumes d'activation pour la diffusion des atomes dans l'or, le cuivre et l'aluminium. *J. Phys. France* **29**, 345–352, DOI: 10.1051/jphys:01968002904034500 (1968).
- **16.** Rein, G. & Mehrer, H. Effect of hydrostatic pressure and temperature on the self-diffusion rate in single crystals of silver and gold. *Philos. Mag. A* **45**, 467–492, DOI: 10.1080/01418618208236183 (1982).
- 17. Rothman, S. J., Peterson, N. L. & Robinson, J. T. Isotope Effect for Self-Diffusion in Single Crystals of Silver. *physica status solidi* (*b*) 39, 635–645, DOI: https://doi.org/10.1002/pssb.19700390231 (1970).
- **18.** Gilder, H. M. & Lazarus, D. Role of vacancy anharmonicity on non-arrhenius diffusional behavior. *Phys. Rev. B* **11**, 4916–4926, DOI: 10.1103/PhysRevB.11.4916 (1975).
- **19.** Varotsos, P., Ludwig, W. & Alexopoulos, K. Calculation of the formation volume of vacancies in solids. *Phys. Rev. B* **18**, 2683–2691, DOI: 10.1103/PhysRevB.18.2683 (1978).
- **20.** Mundy, J. N., Ockers, S. T. & Smedskjaer, L. C. Vacancy migration enthalpy in tungsten at high temperatures. *Philos. Mag. A* **56**, 851–860, DOI: 10.1080/01418618708204493 (1987).
- **21.** Herzig, C., Köhler, U. & Divinski, S. Tracer diffusion and mechanism of non-Arrhenius diffusion behavior of Zr and Nb in body-centered cubic Zr-Nb alloys. *J. Appl. Phys.* **85**, 8119 8130, DOI: 10.1063/1.370650 (1999).
- **22.** Carling, K. *et al.* Vacancies in metals: From first-principles calculations to experimental data. *Phys. Rev. Lett.* **85**, 3862–3865, DOI: 10.1103/PhysRevLett.85.3862 (2000).
- **23.** Glensk, A., Grabowski, B., Hickel, T. & Neugebauer, J. Breakdown of the Arrhenius Law in Describing Vacancy Formation Energies: The Importance of Local Anharmonicity Revealed by Ab initio Thermodynamics. *Phys. Rev. X* **4**, 011018, DOI: 10.1103/PhysRevX.4.011018 (2014).

- **24.** Gong, Y. *et al.* Temperature dependence of the Gibbs energy of vacancy formation of fcc Ni. *Phys. Rev. B* **97**, 214106, DOI: 10.1103/PhysRevB.97.214106 (2018).
- **25.** Mattsson, T. R., Sandberg, N., Armiento, R. & Mattsson, A. E. Quantifying the anomalous self-diffusion in molybdenum with first-principles simulations. *Phys. Rev. B* **80**, 224104, DOI: 10.1103/PhysRevB.80.224104 (2009).
- **26.** Zhang, X., Grabowski, B., Hickel, T. & Neugebauer, J. Calculating free energies of point defects from ab initio. *Comput. Mater. Sci.* **148**, 249–259, DOI: https://doi.org/10.1016/j.commatsci.2018.02.042 (2018).
- 27. Vineyard, G. H. Frequency factors and isotope effects in solid state rate processes. *J. Phys. Chem. Solids* 3, 121–127, DOI: https://doi.org/10.1016/0022-3697(57)90059-8 (1957).
- **28.** Hargather, C. Z., Shang, S.-L., Liu, Z.-K. & Du, Y. A first-principles study of self-diffusion coefficients of fcc Ni. *Comput. Mater. Sci.* **86**, 17–23, DOI: https://doi.org/10.1016/j.commatsci.2014.01.003 (2014).
- **29.** Mantina, M. *et al.* First-principles calculation of self-diffusion coefficients. *Phys. Rev. Lett.* **100**, 215901, DOI: 10.1103/PhysRevLett.100.215901 (2008).
- **30.** Zhang, X. *et al.* Temperature dependence of the stacking-fault Gibbs energy for Al, Cu, and Ni. *Phys. Rev. B* **98**, 224106, DOI: 10.1103/PhysRevB.98.224106 (2018).
- **31.** van de Walle, A., Hong, Q., Kadkhodaei, S. & Sun, R. The free energy of mechanically unstable phases. *Nat. Commun.* **6**, 7559, DOI: 10.1038/ncomms8559 (2015).
- **32.** E, W., Ren, W. & Vanden-Eijnden, E. String method for the study of rare events. *Phys. Rev. B* **66**, 052301, DOI: 10.1103/PhysRevB.66.052301 (2002).
- **33.** Boisvert, G., Mousseau, N. & Lewis, L. J. Surface diffusion coefficients by thermodynamic integration: Cu on cu(100). *Phys. Rev. B* **58**, 12667–12670, DOI: 10.1103/PhysRevB.58.12667 (1998).
- **34.** Swinburne, T. D. & Marinica, M.-C. Unsupervised calculation of free energy barriers in large crystalline systems. *Phys. Rev. Lett.* **120**, 135503, DOI: 10.1103/PhysRevLett.120.135503 (2018).
- **35.** Shapeev, A. V. Moment tensor potentials: A class of systematically improvable interatomic potentials. *Multiscale Model.* & *Simul.* **14**, 1153–1173, DOI: 10.1137/15M1054183 (2016).
- **36.** Jung, J. H., Srinivasan, P., Forslund, A. & Grabowski, B. High-accuracy thermodynamic properties to the melting point from ab initio calculations aided by machine-learning potentials. *npj Comput. Mater.* **9**, 3, DOI: 10.1038/s41524-022-00956-8 (2023).
- **37.** Xu, X., Zhang, X., Ruban, A., Schmauder, S. & Grabowski, B. Strong impact of spin fluctuations on the antiphase boundaries of weak itinerant ferromagnetic ni3al. *Acta Materialia* **255**, 118986, DOI: https://doi.org/10.1016/j.actamat. 2023.118986 (2023).
- **38.** Henkelman, G., Uberuaga, B. P. & Jónsson, H. A climbing image nudged elastic band method for finding saddle points and minimum energy paths. *The J. Chem. Phys.* **113**, 9901–9904, DOI: 10.1063/1.1329672 (2000).
- **39.** Branduardi, D., Gervasio, F. L. & Parrinello, M. From A to B in free energy space. *The J. Chem. Phys.* **126**, 054103, DOI: 10.1063/1.2432340 (2007). https://pubs.aip.org/aip/jcp/article-pdf/doi/10.1063/1.2432340/15394827/054103_1_online.pdf.
- **40.** Forslund, A., Jung, J. H., Srinivasan, P. & Grabowski, B. Thermodynamic properties on the homologous temperature scale from direct upsampling: Understanding electron-vibration coupling and thermal vacancies in bcc refractory metals. *Phys. Rev. B* **107**, 174309, DOI: 10.1103/PhysRevB.107.174309 (2023).
- **41.** Forslund, A. & Ruban, A. Ab initio surface free energies of tungsten with full account of thermal excitations. *Phys. Rev. B* **105**, 045403, DOI: 10.1103/PhysRevB.105.045403 (2022).
- **42.** Montet, G. L. Integral methods in the calculation of correlation factors in diffusion. *Phys. Rev. B* **7**, 650–662, DOI: 10.1103/PhysRevB.7.650 (1973).
- **43.** Blöchl, P. E. Projector augmented-wave method. *Phys. Rev. B* **50**, 17953–17979, DOI: 10.1103/PhysRevB.50.17953 (1994).
- **44.** Perdew, J. P., Burke, K. & Ernzerhof, M. Generalized Gradient Approximation Made Simple. *Phys. Rev. Lett.* **77**, 3865–3868, DOI: 10.1103/PhysRevLett.77.3865 (1996).
- **45.** Kresse, G. & Furthmüller, J. Efficient iterative schemes for ab initio total-energy calculations using a plane-wave basis set. *Phys. Rev. B* **54**, 11169–11186, DOI: 10.1103/PhysRevB.54.11169 (1996).
- **46.** Kresse, G. & Furthmüller, J. Efficiency of ab-initio total energy calculations for metals and semiconductors using a plane-wave basis set. *Comput. Mater. Sci.* **6**, 15–50, DOI: https://doi.org/10.1016/0927-0256(96)00008-0 (1996).

- **47.** Park, J. Y., Huang, H. C. W., Siegel, R. W. & Balluffi, R. W. A quantitative study of vacancy defects in quenched tungsten by combined field-ion microscopy and electrical resistometry. *Philos. Mag. A* **48**, 397–419, DOI: 10.1080/01418618308234901 (1983).
- **48.** Rasch, K.-D., Siegel, R. W. & Schultz, H. Quenching and recovery investigations of vacancies in tungsten. *Philos. Mag. A* **41**, 91–117, DOI: 10.1080/01418618008241833 (1980).
- **49.** Mundy, J. N. Electrical resistivity-temperature scale of tungsten. *Philos. Mag. A* **46**, 345–349, DOI: 10.1080/01418618208239923 (1982).
- **50.** Smedskjaer, L. C., Loper, G. D., Chason, M. K. & Siegel, R. W. Positron annihilation studies of vacancy formation in tungsten, chromium, and niobium. *MRS Online Proc. Libr.* (*OPL*) **41**, 57, DOI: 10.1557/PROC-41-57 (1984).
- **51.** Schaefer, H.-E. Investigation of thermal equilibrium vacancies in metals by positron annihilation. *Phys. Status Solidi (a)* **102**, 47–65, DOI: https://doi.org/10.1002/pssa.2211020104 (1987).
- **52.** Maier, K., Peo, M., Saile, B., Schaefer, H. E. & Seeger, A. High–temperature positron annihilation and vacancy formation in refractory metals. *Philos. Mag. A* **40**, 701–728, DOI: 10.1080/01418617908234869 (1979).
- **53.** Wimmer, E. *et al.* Temperature-dependent diffusion coefficients from ab initio computations: Hydrogen, deuterium, and tritium in nickel. *Phys. Rev. B* **77**, 134305, DOI: 10.1103/PhysRevB.77.134305 (2008).
- **54.** Hooshmand, M., Zhong, W., Zhao, J., Windl, W. & Ghazisaeidi, M. Data on the comprehensive first-principles diffusion study of the aluminum-magnesium system. *Data Brief* **30**, 105381, DOI: https://doi.org/10.1016/j.dib.2020.105381 (2020).
- **55.** Shang, S.-L. *et al.* A comprehensive first-principles study of pure elements: Vacancy formation and migration energies and self-diffusion coefficients. *Acta Materialia* **109**, 128–141, DOI: https://doi.org/10.1016/j.actamat.2016.02.031 (2016).
- **56.** Zhang, X., Grabowski, B., Körmann, F., Freysoldt, C. & Neugebauer, J. Accurate electronic free energies of the 3*d*, 4*d*, and 5*d* transition metals at high temperatures. *Phys. Rev. B* **95**, 165126, DOI: 10.1103/PhysRevB.95.165126 (2017).
- **57.** Glensk, A., Grabowski, B., Hickel, T. & Neugebauer, J. Understanding anharmonicity in fcc materials: From its origin to ab initio strategies beyond the quasiharmonic approximation. *Phys. Rev. Lett.* **114**, 195901, DOI: 10.1103/PhysRevLett. 114.195901 (2015).
- **58.** Gaukel, C. & Schober, H. Diffusion mechanisms in under-cooled binary metal liquids of zr67cu33. *Solid State Commun.* **107**, 1–5, DOI: https://doi.org/10.1016/S0038-1098(98)00176-8 (1998).
- **59.** Laird, B. B. & Schober, H. R. Localized low-frequency vibrational modes in a simple model glass. *Phys. Rev. Lett.* **66**, 636–639, DOI: 10.1103/PhysRevLett.66.636 (1991).
- **60.** Chesser, I. & Mishin, Y. Point-defect avalanches mediate grain boundary diffusion. *Commun Mater* **3**, 90, DOI: https://doi.org/10.1038/s43246-022-00314-7 (2022).
- **61.** Zhu, L.-F. *et al.* Melting properties of the refractory metals V and W and the binary VW alloy fully from first principles. *Phys. Rev. B* **109**, 094110, DOI: 10.1103/PhysRevB.109.094110 (2024).
- 62. CRC Handbook. CRC Handbook of Chemistry and Physics, 88th Edition (CRC Press, 2007), 88 edn.
- **63.** Forslund, A., Jung, J. H., Srinivasan, P. & Grabowski, B. Thermodynamic properties on the homologous temperature scale from direct upsampling: Understanding electron-vibration coupling and thermal vacancies in bcc refractory metals. *Phys. Rev. B* **107**, 174309, DOI: 10.1103/PhysRevB.107.174309 (2023).
- **64.** Andelin, R. L., Knight, J. D. & Kahn, M. Diffusion of tungsten and rhenium tracers in tungsten. *Trans. Met. Soc. AIME* **233**, 19 (1965). (cited from Ref. 12).
- **65.** Pawel, R. & Lundy, T. Tracer diffusion in tungsten. *Acta Metall.* **17**, 979–988, DOI: https://doi.org/10.1016/0001-6160(69) 90042-X (1969).
- **66.** Arkhipova, N. K., Klotsman, S. M., Rabovskii, Y. A. & Timofeyev, A. N. *Fiz. Met. Met.* **43**, 779 (1977). (cited from Ref. 12).
- **67.** Wang, Y., Chen, Z., Windl, W. & Zhao, J.-C. Nonlinear arrhenius behavior of self-diffusion in β -Ti and Mo. *Phys. Rev. Mater.* **6**, 063402, DOI: 10.1103/PhysRevMaterials.6.063402 (2022).
- **68.** Grabowski, B. *et al.* Ab initio vibrational free energies including anharmonicity for multicomponent alloys. *npj Comput. Mater.* **5**, 80, DOI: 10.1038/s41524-019-0218-8 (2019).
- **69.** Zhou, Y. *et al.* Thermodynamics up to the melting point in a TaVCrW high entropy alloy: Systematic *ab initio* study aided by machine learning potentials. *Phys. Rev. B* **105**, 214302, DOI: 10.1103/PhysRevB.105.214302 (2022).

- **70.** Rogal, L. *et al.* Computationally-driven engineering of sublattice ordering in a hexagonal AlHfScTiZr high entropy alloy. *Sci. Reports* **7**, 2209, DOI: 10.1038/s41598-017-02385-w (2017).
- 71. Vaidya, M. *et al.* Phenomenon of ultra-fast tracer diffusion of co in hcp high entropy alloys. *Acta Materialia* 196, 220–230, DOI: https://doi.org/10.1016/j.actamat.2020.06.025 (2020).
- **72.** Sen, S. *et al.* Does Zn mimic diffusion of Al in the HCP Al-Sc-Hf-Ti-Zr high entropy alloys? *Scripta Materialia* **229**, 115376, DOI: https://doi.org/10.1016/j.scriptamat.2023.115376 (2023).
- 73. Sen, S. *et al.* 'Anti-sluggish' Ti diffusion in HCP high-entropy alloys: Chemical complexity vs. lattice distortions. *Scripta Materialia* 224, 115117, DOI: https://doi.org/10.1016/j.scriptamat.2022.115117 (2023).
- **74.** Zhang, X., Divinski, S. & Grabowski, B. *Ab initio* prediction of vacancy energetics in HCP Al-Hf-Sc-Ti-Zr high entropy alloys and the subsystems. *Acta Materialia* **227**, 117677, DOI: https://doi.org/10.1016/j.actamat.2022.117677 (2022).
- **75.** Jung, J. H., Forslund, A., Srinivasan, P. & Grabowski, B. Dynamically stabilized phases with full ab initio accuracy: Thermodynamics of Ti, Zr, Hf with a focus on the hcp-bcc transition. *Phys. Rev. B* **108**, 184107, DOI: 10.1103/PhysRevB. 108.184107 (2023).
- **76.** Parlinski, K., Li, Z. Q. & Kawazoe, Y. First-Principles Determination of the Soft Mode in Cubic ZrO₂. *Phys. Rev. Lett.* **78**, 4063–4066, DOI: 10.1103/PhysRevLett.78.4063 (1997).
- 77. Togo, A. & Tanaka, I. First principles phonon calculations in materials science. *Scripta Materialia* **108**, 1–5, DOI: https://doi.org/10.1016/j.scriptamat.2015.07.021 (2015). Doi: 10.1016/j.scriptamat.2015.07.021.

Acknowledgements

X.Z. thanks Wenchuan Liu for the quasiharmonic calculations and Dr. Axel Forslund for fruitful discussions. Financial support from the European Research Council (ERC) under the European Unions Horizon 2020 research and innovation programme (Grant Agreement No. 865855) is gratefully acknowledged. S.D. and X.Z. acknowledge funding from the Deutsche Forschungsgemeinschaft (DFG) via the research projects DI 1419/24-1 and ZH 1218/1-1. X.Z. and B.G. acknowledge support by the state of Baden-Württemberg through bwHPC and the DFG through grant No. INST 40/575-1 FUGG (JUSTUS 2 cluster) and by the Stuttgart Center for Simulation Science (SimTech).

Author contributions statement

X.Z. designed and conducted the simulations, S.D. checked the comparison with experiment, X.Z. and B.G. analyzed the results and wrote the manuscript. All authors reviewed the manuscript.

Competing interests

The authors declare no competing interests.

Supplementary Material for "Ab initio machine-learning unveils strong anharmonicity in non-Arrhenius self-diffusion of tungsten"

Xi Zhang, ¹ Sergiy V. Divinski, ² and Blazej Grabowski ¹

Institute for Materials Science, University of Stuttgart, D-70569 Stuttgart, Germany

²Institute of Materials Physics, University of Münster, 48149 Münster, Germany

I. TECHNICAL DETAILS

A. DFT calculations

The total energies and forces of configurations selected for training the machine-learning potential as well as the energies of the upsampling snapshots were obtained from DFT calculations. The GGA-PBE exchange-correlation functional was used for all the DFT calculations. A previous ab initio study [1] on temperature-dependent vacancy formation Gibbs energies of Al and Cu showed an outstanding performance of PBE compared to other functionals. The PBE functional was also applied to refractory BCC elements including W in Ref. [2], and a very good prediction of thermodynamic properties up to the melting point was demonstrated, in particular on the homologous temperature scale. In Ref. [2], the Gibbs energy of vacancy formation was also calculated, once at 0 K and additionally at one high-temperature point indicating a strong temperature dependence. In another recent study [3], the melting point of BCC W was calculated with the PBE functional, which enables a comparison with experimental data on the homologous temperature scale. The PBE functional is thus well suited for our present study, and our simulations nicely complement the available literature with the full temperature dependence of formation and migration Gibbs energies for BCC W.

The PAW potential with $5d^46s^2$ valence orbitals from the VASP potential database was used. The plane wave cut-off was set to 250 eV. Supercells based on a $4\times4\times4$ expansion of the conventional BCC unit cell were used (128 atoms for bulk structures and 127 atoms for the vacancy and transition state). A Γ -centered Monkhorst-Pack [4] k-point mesh of $3\times3\times3$ was used for all except the separate quasiharmonic calculations where a mesh of $9\times9\times9$ was applied for convergence. The convergence criterion for the self-consistent electronic loop was specified to be 10^{-5} eV (10^{-6} eV for the quasiharmonic calculations).

Explicit calculations for $G_{\text{form}}(T)$ and $G_{\text{mig}}(T)$ were performed at eight temperatures starting at zero K and going to above the PBE melting temperature of 3349 K [3] (0 K, 600 K 1200 K, 1700 K, 2100 K, 2500 K, 3000 K, and 3400 K), followed by a fourth order polynomial fit. For all calculations, the thermal lattice expansion effect was fully taken into account. The corresponding utilized equilibrium lattice constants are marked in Figure S1(a) on the thermal expansion curves as red

(DFT full) and gray (DFT qh) dots. The equilibrium 0 K lattice constant obtained in this work is $3.1723\,\text{Å}$, slightly larger than the experimental value of $3.16\,\text{Å}$. The relative lattice expansion is displayed in Figure S1(b) in comparison to experimental data.

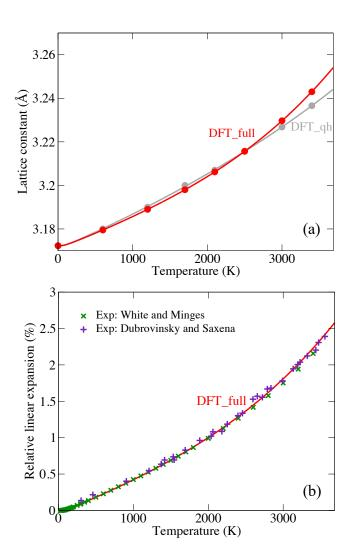


Figure S1. (a) Temperature-dependent lattice constants used in this work. (b) Relative linear lattice expansion compared with experiments: White and Minges [5]; Dubrovinsky and Saxena [6].

B. Nudged elastic band calculations

The transition-state structure $\{\mathbf{R}_I^{\mathrm{sp}}\}$ at a given volume was obtained from DFT-based climbing image nudged elastic band (NEB) [7] calculations implemented in VASP with 11 intermediate images. The spring constant between the images was set to -5 eV/Å^2 . The NEB ionic relaxation with the quasi-Newton algorithm was stopped when all the forces were smaller than 0.05 eV/Å. The total energies of all intermediate images, together with the two end points, were fitted to a force-based cubic spline interpolation using the tangential forces as input to accurately locate the saddle point, as implemented in the VTST-scripts [8].

C. Development of the machine learning potential

1. Potential form

As mentioned in the Methods section, the moment tensor potential (MTP) describes the local chemical environment (see Figure S2) via the radial part f_{μ} containing information about the atomic distances and the angular part $\mathbf{r}_{ij} \otimes ... \otimes \mathbf{r}_{ij}$ containing angular information among the atoms. The radial part is expressed as

$$f_{\mu}(|\mathbf{r}_{ij}|, z_i, z_j) = \sum_{k} c_{\mu, z_i, z_j}^{k} T_k(|\mathbf{r}_{ij}|) (R_{\text{cut}} - |\mathbf{r}_{ij}|)^2, \text{ (S1)}$$

where c_{μ,z_i,z_j}^k are the radial coefficients to be fit, $T_k(|r_{ij}|)$ are the Chebyshev polynomials of order k, and $R_{\rm cut}$ is the cutoff radius (red arrow in Figure S2) beyond which interatomic interactions are not considered. Here, we used a cutoff radius of 5.2 Å covering the 1NN, 2NN, and 3NN neighbor shells of BCC W for all equilibium lattice constants from 0 K to 3400 K, which is sufficient for describing the local environment.

For the angular part, in order to determine the basis set of the potential, one has to setup the so-called "maximum level of moments", lev $_{\rm max}$, defined in Ref. [9] using a notation of "Ng" with N being the value of lev $_{\rm max}$. Generally, the higher the maximum level of moments, the larger the number of basis functions and fitting parameters the MTP model possesses. In this work, a high-level "24g" MTP model (lev $_{\rm max}=24$) containing 912 fitting parameters for the unary tungsten system was selected to ensure accuracy in describing the vibrational space.

2. Training database and active learning

The DFT dataset for training the MTP was obtained from NVT MD snapshots at 3600 K and at four different lattice constants (3.206 Å, 3.227 Å, 3.248 Å, and 3.268 Å) to ensure that a sufficiently large vibrational space can be explored and learned by the MTP.

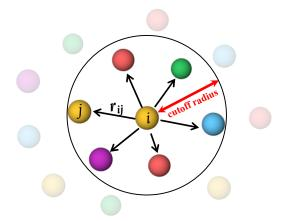


Figure S2. Schematic illustration of the local environment in the MTP model.

An iterative approach according to the "active learning" scheme detailed in Ref. [9] was used to automatically select new configurations to be added in the training set. Based on the D-optimality criterion, an extrapolation grade γ can be calculated for each newly-generated MD snapshot using the so-called maxvol algorithm [9]. The extrapolation grade is a measure of the "novelty" of the new structures compared to the ones already in the training set. From a mathematical point of view, extrapolation by the MTP occurs if γ is greater than unity [9]. The higher the extrapolation grade the severer is the extrapolation by the MTP. During the training process, we used the selection threshold $\gamma_{\text{select}} = 1.1$, i.e., the energies and forces of new configurations with an extrapolation grade larger than 1.1 were calculated by DFT and added to the training set.

The active learning scheme started with an initial MTP trained with 200 bulk MD structures. New MD runs with the MTP obtained in the previous step were performed from which new bulk structures, vacancy structures, and transition state structures were selected and added to the training set. The MTP was then re-trained with the updated training set. The "active learning" procedure stopped when addition of new structures during the MD runs became statistically insignificant. The resulting final training database contained 806 bulk structures, 872 vacancy structures, and 913 transition state structures (2591 in total).

D. Thermodynamic integration

Utilizing the highly-optimized machine learning potential, at each temperature and volume (T,V) point, the thermodynamic integration (TI) from the quasiharmonic potential to the full vibrational moment tensor potential could be efficiently performed using eight λ values, i.e., 0, 0.2, 0.4, 0.6, 0.8, 0.9, 0.95, and 1, followed by a tangent fit. All TI MD simulations were run until a standard error of below 0.05 eV/cell for the resulting free energy

was reached. The Langevin thermostat was used with a friction parameter of 0.01 fs⁻¹ and a time step of 5 fs.

E. Direct upsampling

For the direct upsampling procedure, the number of MTP MD snapshots calculated by DFT for statistical averaging ranged from 360 to 720, depending on the volume and temperature. These numbers are more than one order of magnitude larger than the general upsampling procedure for the bulk ($20{\sim}30$ snapshots for an accuracy of 1 meV/atom). The resulting convergence allows us to reach an accuracy of below 0.2 meV/atom. This very high accuracy per atom translates into an accuracy of about 20 meV/defect.

II. STABILIZATION PARAMETER IN TSTI

To stabilize the reaction coordinate we used $\alpha=1.0$. We tested also $\alpha=0.5$ and 1.5 and plot the resulting $\langle E^{\rm full}-E^{\rm qh}\rangle_{\lambda}$ as a function of λ in Figure S3. Negligible differences are seen. The resulting free energy difference between $\alpha=1.0$ and 1.5 is below 0.2 meV/atom, i.e., in the range of the statistical uncertainty.

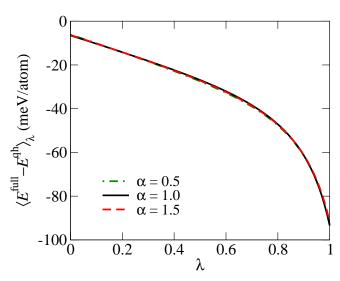


Figure S3. $\langle E^{\text{full}} - E^{\text{qh}} \rangle_{\lambda}$ as a function of λ for three different values of the stabilization parameter α .

III. ELECTRONIC DOS CONVERGENCE

To quantify the uncertainty of the mean eDOS's shown in Figure 4 of the main text, we plot the standard errors in Figure S4(a) and compare them with the differences between different types of structures, i.e., $|eDOS_{bulk}-eDOS_{vac}|$ and $|eDOS_{vac}-eDOS_{ts}|$, in Figure S4(b). While the general features in terms of peaks

and valleys between the standard error and the differences are similar, the values are about one order of magnitude smaller in particular at the valleys and peaks of the eDOS's where the differences shows a peak. This means the mean eDOS's averaged over 120 MD snapshots shown in Figure 4 of the main text are well converged.

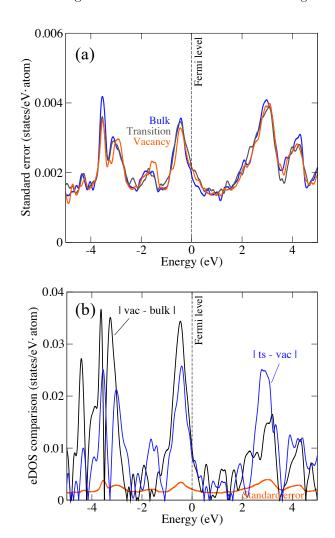


Figure S4. Statistical analysis of the eDOS's: (a) standard errors and (b) comparison between the eDOS differences and the mean standard error.

IV. DIFFUSIVITY ON THE ABSOLUTE TEMPERATURE SCALE

On the absolute temperature scale, while the predicted diffusivity is about two orders of magnitute higher than the experimental data, the general temperature dependence shows a good agreement. We attribute the discrepancy in magnitude to the employed PBE exchange-correlation functional which underestimates the melting point of W by more than 300 K [3].

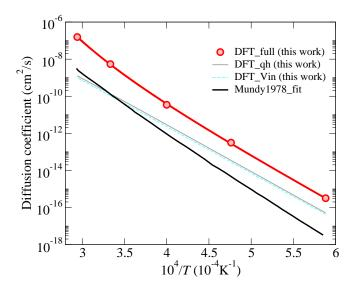


Figure S5. Arrhenius plot of self-diffusivity in bcc tungsten calculated with the proposed *ab initio* machine-learning TSTI approach with all finite-temperature excitations taken into account (red circles and lines) on the absolute temperature scale in comparison to the fitted experimental data from Mundy et al. [10].

V. UNCERTAINTY ANALYSIS

Results of the uncertainty estimation of the target quatities are summarized in Table S1. We focus on the propagation of the statistical uncertainty in each free energy contribution to estimate the total uncertainty of the calculated formation and migration Gibbs energies as well as diffusivities. For each free energy value at the given temperature, following the concept of the Student's t-distribution, the uncertainty δ is calculated as

$$\delta = t_{95\%, n-1} \frac{\sigma}{\sqrt{n}},\tag{S2}$$

where σ and n refer to the standard deviation and the sample size and $t_{95\%,n-1}$ is the two-sided t value of the 95% confidence with n-1 degrees of freedom. According to the propagation of the statistical uncertainty, the total uncertainty of a function of $A \pm B \pm ...$ is calculated as $\sqrt{\delta_A^2 + \delta_B^2 + ...}$, so the uncertainty of the diffusivity can be estimated as

$$\delta_{\text{diff}} = D(T) \sqrt{\delta_{\text{form}}^2 + \delta_{\text{mig}}^2} / (k_B T),$$
 (S3)

where D(T) is the calculated diffusivity and δ_{form} and δ_{form} are the uncertainty of the formation and migration Gibbs energy, respectively.

VI. ON THE DI-VACANCY HYPOTHESIS

In a previous high-accuracy DFT study [1], the divacancy mechanism has been convincingly ruled out

in FCC elements (i.e., Al and Cu) by explicit finite-temperature DFT calculations of di-vacancy formation Gibbs energies. Therein, clear contradictions with experimental observations in terms of the vacancy concentration and the formation entropy were obtained for the di-vacancy hypothesis. For BCC refractory elements like tungsten, due to the significant challenges in experimental measurements of mono- and di-vacancy concentrations at very high temperatures, the same set of arguments as given in Ref. [1] for FCC elements cannot be directly utilized. We thus provide here an alternative analysis based on experimental diffusion data and the available monovacancy and di-vacancy energetics to substantiate that di-vacancies can hardly explain the non-Arrhenius diffusion of BCC W.

By assuming a collective mechanism of diffusion (i.e., mono- and di-vacancies) in BCC W, the diffusivity can be expressed as:

$$D = \frac{c_{1v}}{c_{1v} + 2c_{2v}} D_{1v} + \frac{2c_{2v}}{c_{1v} + 2c_{2v}} D_{2v}$$
(S4)

=
$$f_1 D_{1v,0} \exp\left(-\frac{Q_{1v}}{k_{\rm B}T}\right) + f_2 D_{2v,0} \exp\left(-\frac{Q_{2v}}{k_{\rm B}T}\right)$$
,(S5)

where c_i and D_i (i = 1v or 2v) refer to the concentration of monovacancies (1v) or di-vacancies (2v) and their diffusivity contributions, respectively. Equation (S4) can be rewritten as shown in Eq. (S5), i.e., in terms of the fraction f_i of each type i of vacancy, the pre-factor $D_{i,0}$, and the activation energy Q_i . Fitting the measured diffusivities to Eq. (S5), as shown in Ref [10], results in (in cm²/s):

$$D = 0.04 \exp\left(-\frac{5.45 \text{ eV}}{k_{\rm B}T}\right) + 46 \exp\left(-\frac{6.9 \text{ eV}}{k_{\rm B}T}\right), \text{ (S6)}$$

where the first term would correspond to the monovacancy diffusion since the activation energy (5.45 eV) agrees well with the sum of the mean values of the available experimental data for the mono-vacancy formation energy (3.8 eV) and migration energy (1.7 eV). It must be then that the second term would correspond to divacancy diffusion; however, in such a case a clear contradiction can be derived as follows.

The activation energy of the di-vacancy diffusion Q_{2v} can be written in terms of the mono-vacancy formation energy $H_{\rm form}^{1v}$, the binding energy of a vacancy pair $H_{\rm bind}^{2v}$, and the di-vacancy migration energy $H_{\rm mig}^{2v}$ as

$$Q_{2v} = 2H_{\text{form}}^{1v} - H_{\text{bind}}^{2v} + H_{\text{mig}}^{2v}.$$
 (S7)

The di-vacancy binding energy then reads

$$H_{\text{bind}}^{2v} = 2H_{\text{form}}^{1v} + H_{\text{mig}}^{2v} - Q_{2v}.$$
 (S8)

The experimental di-vacancy migration energy was reported by Park et al. [11] and by Rasch et al. [12] to be very similar to the mono-vacancy migration energy, i.e., about 1.8 eV. This was also confirmed by a recent DFT-based kinetic Monte Carlo study [13] where an effective

\overline{T}	Bulk				Vacancy				Transition state				~	~	\overline{D}
(K)	$\Delta F^{\mathrm{qh} \to \mathrm{full}}$	ΔF^{up}	F^{el}	Total	$\Delta F^{\mathrm{qh} \to \mathrm{full}}$		F^{el}	Total	$\Delta F^{\mathrm{qh} o \mathrm{full}}$	ΔF^{up}	F^{el}	Total	$G_{ m form}$	$G_{ m mig}$	(cm^2/s)
600	0	0.004	0.001	0.004	0	0.005	0.001	0.005	0	0.01	0.001	0.01	0.007	0.012	-
1200	0.002	0.008	0.006	0.01	0	0.015	0.005	0.016	0	0.01	0.005	0.012	0.02	0.02	-
1700	0.005	0.014	0.009	0.017	0.006	0.01	0.01	0.017	0.007	0.01	0.014	0.02	0.024	0.026	1.7×10^{-16}
2100	0.01	0.01	0.017	0.023	0.02	0.012	0.016	0.028	0.01	0.01	0.017	0.023	0.036	0.036	2.0×10^{-13}
2500	0.02	0.014	0.022	0.033	0.013	0.018	0.022	0.031	0.03	0.016	0.026	0.044	0.045	0.054	2.5×10^{-11}
3000	0.024	0.015	0.026	0.038	0.013	0.016	0.029	0.036	0.028	0.016	0.03	0.045	0.052	0.057	3.5×10^{-9}
3400	0.013	0.019	0.04	0.046	0.004	0.02	0.034	0.04	0.033	0.024	0.038	0.056	0.06	0.068	1.0×10^{-7}

TABLE S1. Estimation of the uncertainties. All energy uncertainties are in units of eV/cell.

di-vacancy migration energy of 1.65 eV was obtained. Based on these experimental mono-/di-vacancy energies together with the di-vacancy diffusion activation energy reported by Mundy et al. [10], the di-vacancy binding energy can be calculated as

$$\begin{array}{ll} H_{\rm bind}^{2v} &= 2 H_{\rm form}^{1v} + H_{\rm mig}^{2v} - Q_{2v} \\ &= 2 \times 3.8 \ {\rm eV} + 1.8 \ {\rm eV} - 6.9 \ {\rm eV} = 2.5 \ {\rm eV.(S9)} \end{array}$$

Now, the value of $H_{\rm bind}^{2v}=2.5$ eV is, however, dramatically larger than directly obtained theoretical and experimental values: DFT studies have shown very small divacancy binding energies ranging from -0.1 eV to +0.05 eV (see Ref. [13]). With our own DFT calculations, we also obtained a small 0 K binding energy of -0.01 eV. The only available experimental value is 0.7 eV reported by Park et al [11], which is still well below 1 eV. Such a large discrepancy with respect to the value in Eq. (S9) cannot be explained by uncertainty. Therefore, the divacancy diffusion mechanism cannot be used to explain the non-Arrhenius diffusion of BCC W, or at least it must be that it only plays a minor role.

In fact, the consistent curvature of the full DFT results with experiment obtained in the present study based on a single mono-vacancy mechanism is clear and convincing evidence that the di-vacancy mechanism contribution is not appropriate in explaining the non-Arrhenius dependence.

VII. MIGRATION PATHWAY AT HIGH TEMPERATURES

Figure S6 depicts 754 migration pathways collected from MTP-MD runs at 3400 K (the highest temperature considered in this work) where the gray dots indicate the trajectories of atoms at the BCC corners vibrating and migrating toward the vacancy in the middle of the BCC unit cell (cube with the black edges). It is apparent that, on average, the migration pathways of the eight nearest neighbors of the vacancy preserve the full BCC crystalline symmetry, migrating along the $\langle 111 \rangle$ direction which is the same as for the NEB path at 0 K.

Moreover, we show the distribution density at the right bottom corner by cross-sections cut by the (110) plane and the (111) plane. The resulting statistical Gaussian distributions are centered along the [111] direction, thus further supporting that at high temperatures the migration pathways follow the 0 K NEB pathway within an ensemble average. This is due to the fact that for a symmetrical crystalline structure like BCC, the full symmetry needs to be preserved even at high temperatures. The distribution density shown in Figure S6 agrees well with the description of the finite temperature string method that the finite-temperature trajectories can be described as a tube in configuration space. The tube center gives the reaction coordinate and results from the average over all trajectories.

VIII. DIRECT MTP MD SIMULATIONS

In order to further validate the TSTI approach, for three selected high temperatures, i.e., 3000 K, 3200 K, and 3400 K, we performed explicitly direct MD simulations using the optimized MTP, from which the self-diffusivity of W can be extracted via

$$D = \frac{\langle R^2 \rangle}{6t} \tag{S10}$$

where $\langle R^2 \rangle$ is the mean squared displacement of the diffusing atom and t is the time.

MTP MD simulations were performed with LAMMPS [14] utilizing a simulation box comprised of 1024 atoms (8 \times 8 \times 8 expansion of the BCC unit cell) where a single vacancy was introduced. The DFT-predicted expanded lattice constants were used. For each selected temperature, 50 independent NVT MD runs were carried out for 20 ns using the Nose-Hoover thermostat with a damping parameter of 100 fs. The time step was set to be 1 fs.

The mean squared displacement as a function of time obtained at 3400 K is shown in Figure S7 as an example. The resulting diffusivities from direct MTP MD simulations are shown in Figure S8 and compared with the MTP TSTI results. Both are rescaled by the DFT-predicted vacancy concentrations at the selected temperatures by assuming that diffusivities are in proportion to the vacancy concentration. It is clear that diffusivities computed from both methods agree very well not only in

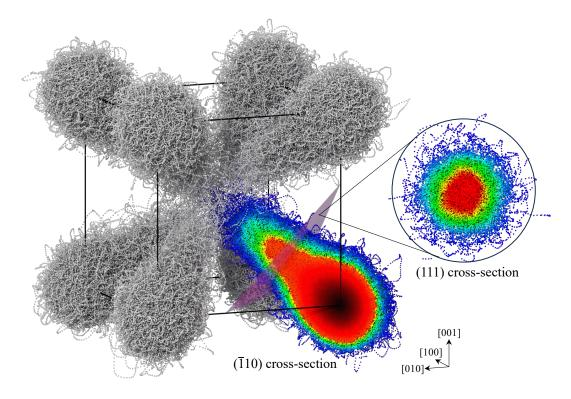


Figure S6. Statistical plot of 754 migration pathways for BCC W collected from MTP-MD at 3400 K.

the absolute values but also in the temperature dependence. This highlights the validity of the present TSTI computational framework and its high predictive power and accuracy.

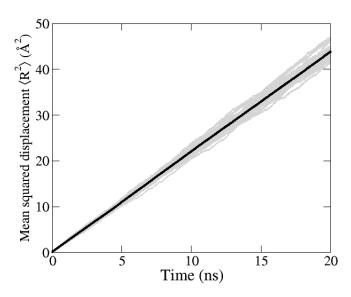


Figure S7. Mean squared displacement as a function of time at $3400~\rm K$. Gray lines are the results of each independent MD run (50 in total) and the black line shows the mean values.

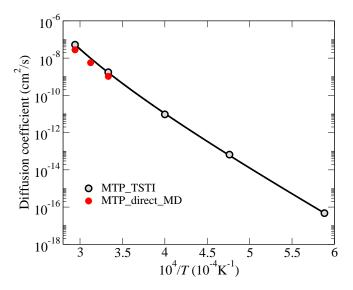
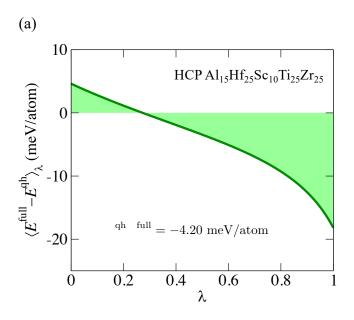


Figure S8. Arrhenius plot of self-diffusivity computed from the present TSTI approach and direct MD simulations using MTP.

IX. APPLICATION OF TSTI IN HIGH-ENTROPY ALLOYS

First TSTI results for a five-component HCP high entropy alloy (HEA), $Al_{15}Hf_{25}Sc_{10}Ti_{25}Zr_{25}$, are shown in Figure S9. The HEA was modeled with a special quasirandom structure with 95 atoms ($4\times4\times3$ expan-



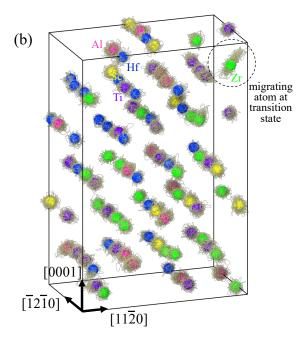


Figure S9. (a) $\langle E^{\text{full}} - E^{\text{qh}} \rangle_{\lambda}$ as a function of λ for Zr diffusion at the transition state in an HCP Al₁₅Hf₂₅Sc₁₀Ti₂₅Zr₂₅ HEA calculated at 1000 K. Integration of the green line (green shaded area) gives the anharmonic free energy (with MTP accuracy) shown in the figure. (b) Illustration of the stable MD trajectory (silver lines; 10000 steps).

sion of the conventional HCP unit cell; cf. Figure S9(b)). The anharmonic free energy of a Zr atom at the transition state (encircled in the figure) was investigated with TSTI at 1000 K. Specifically, the full λ dependence of $\langle E^{\rm full} - E^{\rm qh} \rangle_{\lambda}$ from a quasiharmonic reference to an MTP

(RMSE of 2.5 meV/atom) was calculated and is plotted in Figure S9(a). All transition-state trajectories entering the calculation are stable and the resulting curve is well-behaved. These results substantiate the robust performance of the TSTI approach also for chemically complex materials.

- A. Glensk, B. Grabowski, T. Hickel, and J. Neugebauer, Breakdown of the Arrhenius Law in Describing Vacancy Formation Energies: The Importance of Local Anharmonicity Revealed by Ab initio Thermodynamics, Physical Review X 4, 011018 (2014).
- [2] A. Forslund, J. H. Jung, P. Srinivasan, and B. Grabowski, Thermodynamic properties on the homologous temperature scale from direct upsampling: Understanding electron-vibration coupling and thermal vacancies in bcc refractory metals, Phys. Rev. B 107, 174309 (2023).
- [3] L.-F. Zhu, P. Srinivasan, Y. Gong, T. Hickel, B. Grabowski, F. Körmann, and J. Neugebauer, Melting properties of the refractory metals V and W and the binary VW alloy fully from first principles, Phys. Rev. B 109, 094110 (2024).
- [4] H. J. Monkhorst and J. D. Pack, Special points for brillouin-zone integrations, Physical Review B 13, 5188 (1976).
- [5] G. K. White and M. L. Minges, Thermophysical properties of some key solids: An update, International Journal of Thermophysics 18, 1269 (1997).
- [6] L. S. Dubrovinsky and S. K. Saxena, Thermal Expansion of Periclase (MgO) and Tungsten (W) to Melting Temperatures, Physics and Chemistry of Minerals 24, 547

(1997).

- [7] G. Henkelman, B. P. Uberuaga, and H. Jónsson, A climbing image nudged elastic band method for finding saddle points and minimum energy paths, The Journal of Chemical Physics 113, 9901 (2000).
- [8] G. Henkelman and H. Jónsson, Improved tangent estimate in the nudged elastic band method for finding minimum energy paths and saddle points, The Journal of Chemical Physics 113, 9978 (2000).
- [9] I. S. Novikov, K. Gubaev, E. V. Podryabinkin, and A. V. Shapeev, The MLIP package: moment tensor potentials with MPI and active learning, Machine Learning: Science and Technology 2, 025002 (2021).
- [10] J. N. Mundy, S. J. Rothman, N. Q. Lam, H. A. Hoff, and L. J. Nowicki, Self-diffusion in tungsten, Physical Review B 18, 6566 (1978).
- [11] J. Y. Park, H. C. W. Huang, R. W. Siegel, and R. W. Balluffi, A quantitative study of vacancy defects in quenched tungsten by combined field-ion microscopy and electrical resistometry, Philosophical Magazine A 48, 397 (1983).
- [12] K.-D. Rasch, R. W. Siegel, and H. Schultz, Quenching and recovery investigations of vacancies in tungsten, Philosophical Magazine A 41, 91 (1980).

- [13] K. Heinola, F. Djurabekova, and T. Ahlgren, On the stability and mobility of di-vacancies in tungsten, Nuclear Fusion **58**, 026004 (2017).
- [14] A. P. Thompson, H. M. Aktulga, R. Berger, D. S. Bolintineanu, W. M. Brown, P. S. Crozier, P. J. in 't Veld, A. Kohlmeyer, S. G. Moore, T. D. Nguyen, R. Shan,

M. J. Stevens, J. Tranchida, C. Trott, and S. J. Plimpton, LAMMPS - a flexible simulation tool for particle-based materials modeling at the atomic, meso, and continuum scales, Comp. Phys. Comm. **271**, 108171 (2022).